

Comparative annealing effect on bonded wafers in air and ultrahigh vacuum for microelectromechanical systems/microfluidics packaging

Matiar M. R. Howlader
McMaster University
Department of Electrical and Computer
Engineering
Hamilton, Ontario L8S 4K1, Canada

Tadatomo Suga
University of Tokyo
Department of Precision Engineering
Tokyo 113-8656, Japan

Abstract. The fundamentals of room temperature bonding methods—surface activated bonding (SAB) and sequentially plasma-activated bonding (SPAB)—are reviewed with applications for packaging of microelectromechanical systems (MEMS) and microfluidic devices. The room temperature bonding strength of the silicon/silicon interface in the SAB and SPAB is as high as that of the hydrophilic bonding method, which requires annealing as high as 1000°C to achieve covalent bonding. After heating, voids are not observed and bonding strengths are not changed in the SAB. In the SPAB, interfacial voids are increased and decreased the bonding strength. Water rearrangement such as absorption and desorption across the bonded interface is found below 225°C. While voids are not significant up to 400°C, a considerable amount of thermal voids above 600°C is found due to viscous flow of oxides. Before heating, interfacial amorphous layers are observed both in the SAB (8.3 nm) and SPAB (4.8 nm), but after heating these disappear and enlarge in the SAB and SPAB, respectively. This enlarged amorphous layer is SiO₂, which is due to the oxidation of silicon/silicon interface after sequential heating. The bonding strength, sealing, and chemical performances of the interfaces meet the requirements for MEMS and microfluidics applications. © 2010 Society of Photo-Optical Instrumentation Engineers. [DOI: 10.1117/1.3500747]

Subject terms: sequential plasma activated bonding; bonding strength; void; viscous flow; nanointerface; electron energy loss spectroscopy; sealing; chemical performance.

Paper 10013SSPR received Mar. 2, 2010; revised manuscript received Aug. 18, 2010; accepted for publication Oct. 26, 2010; published online Oct. 00, 2010.

1 Introduction

Packaging often appears as a limiting factor when moving research and design concepts to working prototypes such as microelectromechanical systems (MEMS). Room temperature direct bonding for MEMS and microfluidic devices packaging is now regarded as enabling technologies that are applicable to a large variety of MEMS projects and structures, and for demonstrating novel packaging. Since the bonding process is often the last step of packaging processes for MEMS devices, high temperature processing for bonding is not possible at that stage because of thermal mismatch problems and gas formation in the cavities that degrade device performance. MEMS devices are interfaced with real-world systems and respond to incoming signals.^{1,2} In addition, many MEMS devices such as resonators, accelerometers, etc., require hermetic vacuum sealing or controllable cavity pressure³ to protect them from harsh environments, internal gases, mechanical damage, and contaminations. Furthermore, MEMS devices may require no-load or low-load bonding methods because of the delicate nature of their structure.^{4,5} Finally, it is well known that the packaging cost is about 70% of the total fabrication cost for devices, which can be reduced by wafer-level packaging.⁶ Therefore, there is a significant demand for low temperature wafer-level bonding techniques for MEMS packaging.

Two room temperature surface-activation-based bonding methods, surface activated bonding (SAB) and sequential plasma activated bonding (SPAB), have been demonstrated for packaging of MEMS, microfluidic, and optoelectronic devices.⁷ In the SAB method, two smooth surfaces are cleaned by using an argon fast atom beam (Ar-FAB) in an ultrahigh vacuum (UHV), followed by contact in vacuum. The SPAB combines the physical sputtering effect of reactive ion etching (RIE) plasma with the chemical reactivity of microwave (MW) radicals. Two activated wafers are contacted in air. Figure 1 shows the schematic diagram of the SAB and SPAB methods. In the SAB, the strong adhesion between two mated surfaces occurs because of the clean, smooth, and activated surfaces treated with Ar-FAB. In SPAB, spontaneous bonding occurs because of the concurrent removing of surface contaminants and native oxides, and depositing of oxides or nitrides on the activated surfaces. This process provides a high reactive surface that allows spontaneous bonding at room temperature.⁸ The SAB and SPAB methods both offer a high bonding strength equivalent to that of bulk materials without annealing.

One of the issues with the bonding methods is the voids or unbonded regions at the interface. Voids control the reliability of the bonded interface such as bonding strength and hermeticity. Voids mainly attribute to the presence of surface particles, contaminants (i.e., hydrocarbon and metal ions from tweezers), reaction byproducts (i.e., H₂O and H₂), and plasma-induced defects. Nucleation of voids can

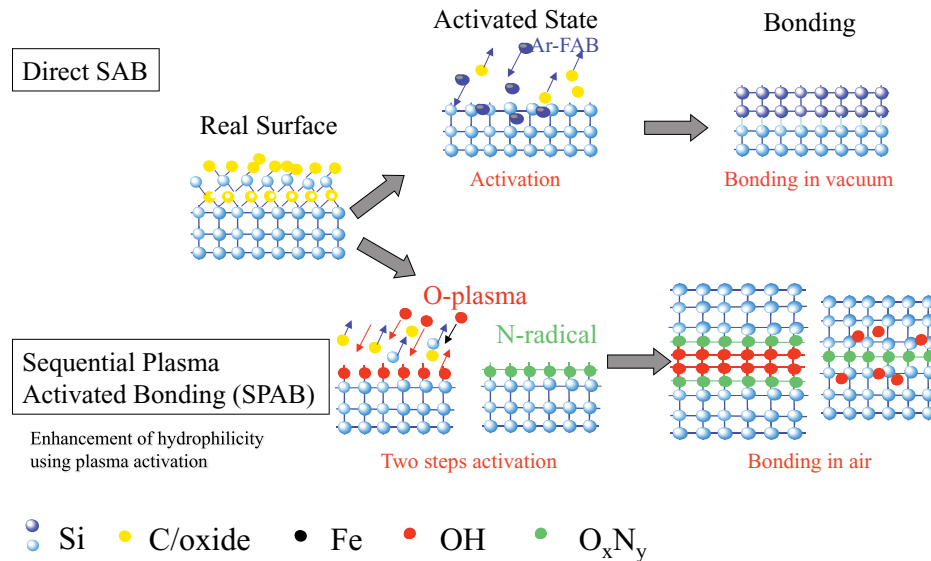


Fig. 1 Schematic diagram of surface-activated bonding (SAB) and sequential plasma-activated bonding (SPAB) methods. In both methods, high bonding strength is achieved without heating. In SAB, dangling sites of the activated surfaces adhere to each other. In SPAB, high reactive hydrophilic surfaces are strong at room temperature.

82 accelerate during the fabrication process flow at higher tem- 118
 83 peratures in some applications. For example, in smart-cut 119
 84 processes to fabricate silicon-on-insulator (SOI) substrates, 120
 85 ion-implanted and bonded specimens go through a high tem- 121
 86 perature annealing step, which is required for layer transfer.⁹ 122
 87 Hence, study on the nucleation of voids at the bonded inter- 123
 88 face with different processing conditions such as plasma pa- 124
 89 rameters, annealing environment, and temperature is needed. 125

90 Previously the sequentially plasma-activated silicon 126
 91 bonded wafers showed that the bonding strengths were re- 127
 92 duced after annealing in air.¹⁰ The cause of the reduction of 128
 93 the bonding strength was believed due to the formation of 129
 94 voids and brittle oxide layers across the interface. While the 130
 95 quality (i.e., tensile strength) of the bonded interface was in- 131
 96 vestigated after annealing, the cause of the reduction of bond- 132
 97 ing strength after annealing was not investigated in terms of 133
 98 the void nucleation at the interface. On the other hand, the 134
 99 void nucleation as well as its relationship with the bonding 135
 100 strength in the SAB has not been investigated yet. In addition 136
 101 to these behaviors of the interface, chemical and hermetic 137
 102 sealing reliability is very important for the proper function- 138
 103 ing of MEMS and microfluidic device packaging. However, a 139
 104 comparative study of the performance of the bonded interface 140
 105 created by SAB and SPAB has not been done yet. 141

106 This work reports on a systematic investigation of the per- 142
 107 formance of the silicon/silicon bonded interface fabricated by 143
 108 using SAB and SPAB. The bonding results include the bond- 144
 109 ing strength measured by tensile pulling tests, voids observed 145
 110 by infrared (IR) transmission images, and nanostructure of 146
 111 the interface performed by high resolution transmission elec- 147
 112 tron microscopy (HRTEM) in different heating temperatures. 148
 113 Also, the hermetic sealing and chemical reliability of the in- 149
 114 terface has been reviewed. 150

115 2 Experimental Procedure

116 Commercially available one-side polished 50-, 100-, and 152
 117 200-mm silicon (100) wafers were used. The thicknesses 153
 154
 155

of the wafers were 275 ± 25 , 525 ± 25 , and $730 \mu\text{m}$, respec- 118
 tively. The wafers were p-type and the resistivity was 20 119
 to $30 \Omega \cdot \text{cm}$. Rectangular cavities and microchannel struc- 120
 tures were fabricated on the wafer-level samples by using the 121
 standard bulk micromachining processes. 122

In the SAB processes, a wafer-level robot-controlled SAB 123
 tool was utilized for the bonding experiments. It consists 124
 of a transfer chamber surrounded by processing, analyzing, 125
 heating, turning over/preliminary alignment (prealignment), 126
 alignment/preliminary bonding (prebonding), and bonding 127
 chambers. The tool is capable of eight wafers. The silicon 128
 wafers were loaded into the load lock chamber and then 129
 activated separately in the processing chamber by Ar-FAB 130
 with a voltage of 1.45 kV and 48 mA for 300 s unless other- 131
 wise mentioned. The background and process pressures were 132
 1.4×10^{-9} and 4.2×10^{-4} Torr. More details of the SAB 133
 tool can be found in Ref. 2. 134

The sequential plasma activation of silicon surfaces was 135
 accomplished using newly developed hybrid plasma bond- 136
 ing (HPB), as shown in Fig. 2. The wafer-level HPB system 137
 consists of plasma activation and anodic bonding chambers. 138
 For this study, only a plasma activation chamber was used. 139
 The plasma activation chamber is equipped with reactive ion 140
 etching (RIE) and microwave (MW) plasma sources. The 141
 plasma activation chamber is separated into top and bottom 142
 compartments by an ion trapping metallic plate. The RIE 143
 and MW plasma were sequentially generated using O₂ and 144
 N₂ gases at the bottom and top compartments, respectively. 145
 The ion trapping metallic plate has 1-mm-diam holes, which 146
 trap charged ions. Therefore, MW plasma generates electri- 147
 cally neutral ions at the bottom compartment. The RIE and 148
 MW plasmas were generated at a frequency of 13.56 MHz 149
 and 2.45 GHz, respectively. Details of the sequential plasma 150
 activation can be found in Ref. 7. 151

The specimens of groups A and B show the plasma pa- 152
 rameters to investigate the influence of O₂ RIE plasma time 153
 and power in the SPAB, respectively (Table 1). After plasma 154
 activation, the wafers were taken out of the chamber and 155

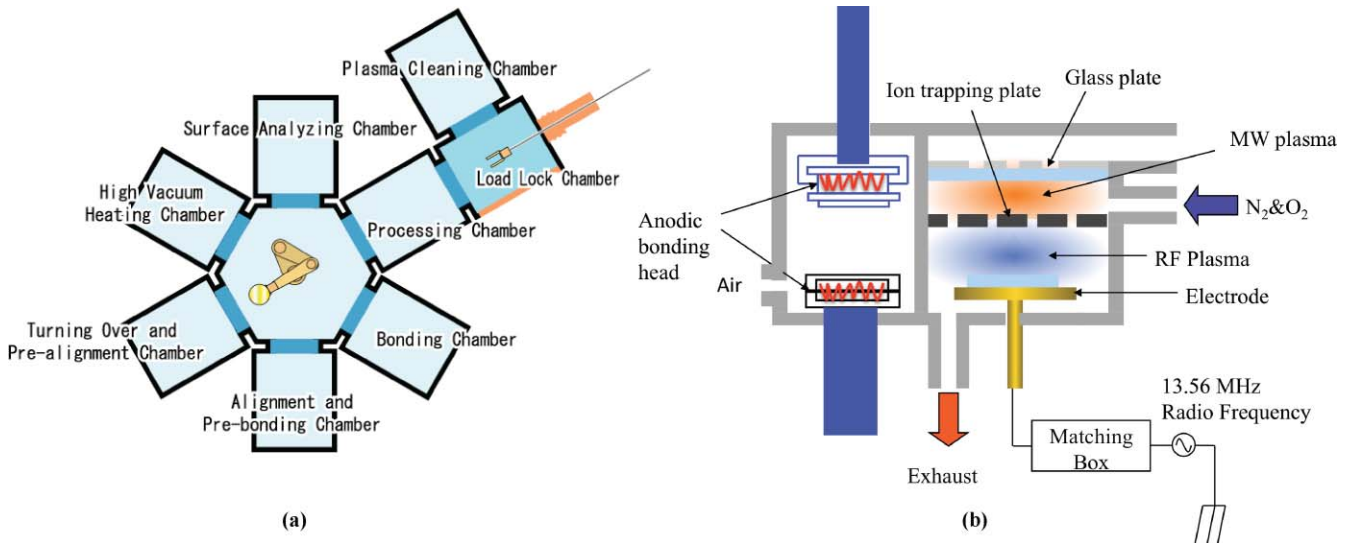


Fig. 2 Schematic diagram of the SAB, and hybrid plasma bonding (HPB) systems.^{2,8}

156 bonded together by applying pressure manually. Finally, the
 157 bonded specimens were cold-rolled under 0.2-MPa pressure
 158 at room temperature to remove trapped air.

159 To investigate the influence of postbond annealing, the
 160 bonded specimens were annealed following a predefined
 161 annealing profile, which is discussed later. An infrared (IR)
 162 transmission method was used to investigate the voids in
 163 the silicon/silicon-bonded interface affected by different
 164 O₂ RIE times, powers, and annealing temperatures. For
 165 tensile strength measurements, the bonded specimens were
 166 diced into sizes of 10 × 10 mm. The diced pieces were glued
 167 with copper jigs, and the tensile strength was measured using
 168 an Instron (Norwood, Massachusetts) tensile tester. Specimens
 169 for HRTEM were prepared from the bonded pairs by
 170 standard procedures including dicing, polishing, dimpling,
 171 and ion milling. To investigate the elemental composition
 172 at the bonded interface, electron energy loss spectroscopy
 173 (EELS) was performed.

Table 1 Plasma parameters used for silicon surface activation.

Specimen number	O ₂ RIE plasma			N ₂ MW radical		
	Power (W)	Time (s)	Pressure (pa)	Power (W)	Time (s)	Pressure (pa)
A1		15				
A2	200	30	60	2500	30	60
A3		60				
B1	200					
B2	300	30	60	2500	15	60
B3	400					

3 Results and Discussion

3.1 Annealing Effect on Bonding Strength

174 In the SAB and SPAB methods, silicon wafers spontaneously
 175 bond on the activated surfaces without annealing.¹⁰ On the
 176 other hand, hydrophilic bonding results from interaction be-
 177 tween silanol (SiOH) groups formed on the surface, and
 178 requires annealing at high temperatures to achieve a bond-
 179 ing strength equivalent to that in the SPAB.^{11,12} The bond-
 180 ing strength of silicon/silicon as a function of annealing
 181 temperature in the SAB and SPAB compared with the hy-
 182 drophilic bonding methods is shown in Fig. 3.^{13,14} The av-
 183 erage bonding strength with standard deviation values are
 184 plotted for the SPAB method. In hydrophilic bonding, the
 185 bonding strength increased with the increase in annealing
 186 temperatures at different slopes. First, the bonding strength
 187
 188

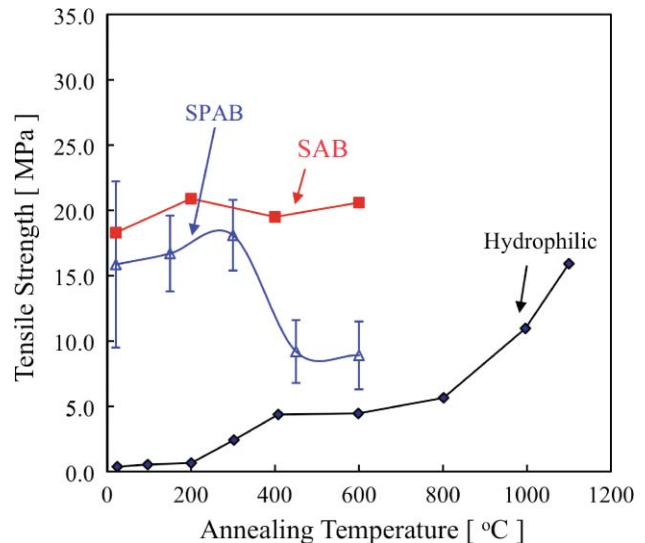


Fig. 3 Comparison of tensile strengths of silicon/silicon wafers in the SAB, SPAB, and hydrophilic bonding methods as a function of annealing temperature.^{10,13,14}

monotonously changed from room temperature to 200°C, then it changed relatively with higher increasing rates up to 400°C. After that, it changed relatively with lower increasing rates up to 800°C, and finally increased with higher slope up to 1100°C. Before annealing, the bonding strengths of the specimens both in SAB and SPAB were higher than the bonding strength in hydrophilic bonding at 1100°C. After annealing up to 600°C, there is no significant influence on the bonding strengths in the SAB. In the SPAB methods, the bonding strengths increased with the increase in annealing temperature up to 300°C. After that, the bonding strengths decreased with the increase in annealing temperature. These characteristic differences in the bonding strength are attributed to the discrepant mechanisms of void nucleation relevant to the surface behavior across the interfaces. In previous studies, the rearrangement of water that causes void formation across the hydrophilic interface has been investigated.^{12,15} Therefore, a comparative study of void nucleation in SAB and SPAB is investigated as a function of annealing temperature.

3.2 Annealing Effect on Interfacial Voids

To investigate the role of annealing on the nucleation of voids, the 50-mm Si/Si wafers bonded by the SAB method and 100-mm Si/Si wafers bonded by the SPAB method (B2, as shown in Table 1) were sequentially heated up to 600°C in air and nitrogen environments, respectively. The surface activation time was 60 s by Ar-FAB in the SAB. Before heating, the IR images were taken for the specimens. Then, the specimens were heated at 200, 400, and 600°C. The in-

terfaces were observed after each heating step using an IR transmission camera. At all three temperatures, the 50-mm Si/Si wafers were heated for one hour with a ramping rate of 200°C per hour in air. For the specimen of B2, the heating time was four hours with a ramping rate of 200°C per hour in nitrogen environments with a nitrogen flow rate of 90 standard cubic centimeters per minute (scm). Two typical examples of heating dependence of void evolution in SAB and SPAB are shown in Fig. 4¹⁶ before heating and after heating at 600°C. In the SAB, thermal and plasma-induced voids were not observed. The white areas across the edge of the bonded interface are open areas due to blade tests. The void-free interface is in contrast to thermal and plasma-induced voids observed in the SPAB.

In the SPAB, a considerable number of plasma-induced voids was observed before heating. The plasma-induced defect sites such as nanopores and craters were responsible for the voids.¹⁶ After heating, the interfacial voids were not significantly changed up to 400°C in the SPAB. From 600°C, new voids appear due to thermal annealing (now termed thermal voids) with the presence of the original voids due to plasma processing (termed as plasma voids). In fact, the reduction of bonding strength at 450°C indicates that the thermal voids generate below 600°C (Fig. 3). The size and shape of the voids at the SPAB interface were increased with the increase in heating temperature. The size and shape of a few plasma voids were changed with a few Newton rings. The sizes of thermal voids were much bigger compared to that of the plasma voids. The nucleation of thermal voids is attributed to the generation of hydrogen gas from the oxidation reaction of silicon by the adsorbed water.¹⁷ Voids become bubbles (bigger voids) by accumulating voids due to viscous flow of oxides above 400°C.¹⁶ From 600°C, perfectly bonded regions surrounded the thermal voids. No transitions for void evolutions were observed after 600°C. Therefore, further annealing at higher temperatures neither generated the voids nor changed the size and shape. A comparison of the IR images at 600, 800, and 900°C¹⁶ indicates that once the size and shape of the voids are defined at 600°C, they cannot be changed by thermal viscous flow because of high bonding strength at the surrounding areas of the voids already formed at 600°C. The nucleated sites of voids were mainly centered at the plasma-induced defect sites. The plasma-induced defects sites were responsible for the severe reduction of bonding strength for the specimens after heating.

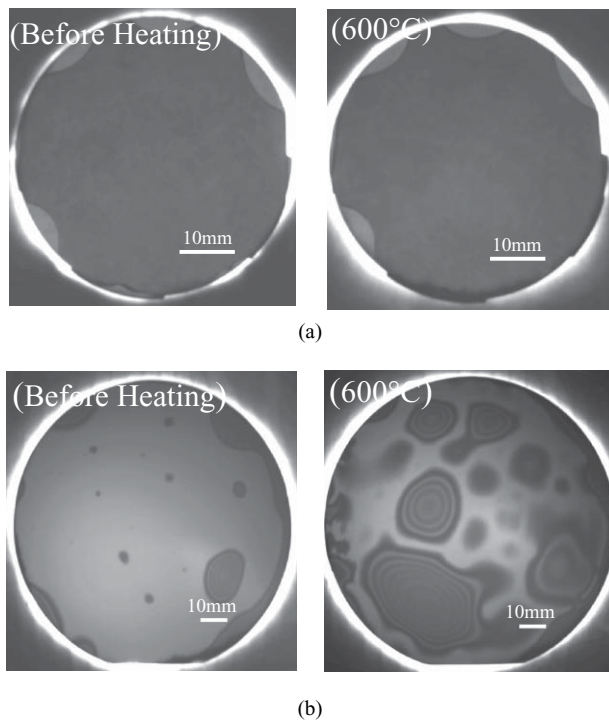


Fig. 4 IR transmission images of silicon/silicon interfacial voids prepared by (a) SAB and (b) SPAB before heating and after sequential heating at 600°C.^{13,16}

3.3 Annealing Effect on Nanointerface

To correlate the transitions of macroscale voids with the nanometer scale interfacial behavior, HRTEM has been performed for the specimens before and after heating. Figure 5 shows the temperature dependence of HRTEM images of silicon/silicon bonded interfaces prepared by the SPAB and SAB. The SPAB specimens were sequentially heated. In both methods, an intermediate amorphous layer at the bonded interface was observed. In the SPAB, the thickness of the interfacial amorphous layer thickness was ~ 4.8 nm before heating. After heating, while the amorphous layer thickness remained constant after heating at 200 and 400°C, it increased to 13-nm thickness after heating at 600°C. The sudden increase in the amorphous layer at 600°C can be correlated with the sudden increase in void density observed from IR

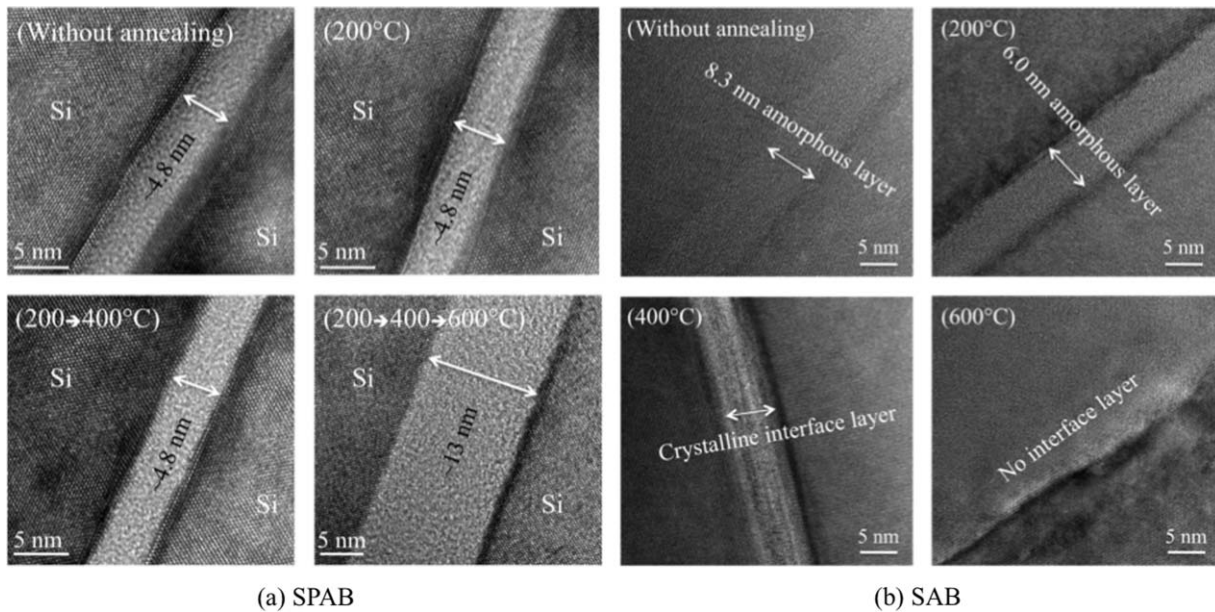
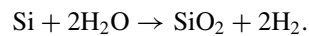


Fig. 5 HRTEM images of silicon/silicon interfaces in (a) SPAB and (b) SAB before heating and after heating up to 600°C. In SPAB, the specimens were sequentially heated.^{8,13}

transmission images.¹⁶ This is caused by: 1. the breaking of SiO_xN_y , and 2. viscous flow of H_2 gas generated from adsorbed H_2O from bulk silicon.⁸ In addition, high concentration of oxygen interstitials in CZ silicon¹⁰ can be responsible for the increased thickness. Due to small amount of SiO_xN_y at the interface, the abrupt change in amorphous layer thickness can be correlated with the oxidation of silicon by the absorbed water onto the plasma-activated silicon surfaces as

follows:



Therefore, the reaction product SiO_2 is responsible for the abrupt change in amorphous layer thickness, and reaction byproduct H_2 is responsible for the nucleation of thermal voids across the interface at 600°C.

In the SAB, the thickness of the interfacial amorphous layer thickness was ~8.3 nm before heating. After heating at 200°C, the amorphous layer was decreased to ~6.0 nm. After heating at 400 and 600°C, the amorphous layer was diminished. This behavior is in contrast to that in the SPAB because of the absence of trapped air/oxides at the interface in the SAB.

3.4 Nanointerfacial Behavior at Low Temperature (50 to 225°C) Annealing

In the SPAB, although the thermal voids were insignificant up to 400°C, the rearrangement of OH molecules at the interface as well as their reactions with silicon would happen. To clarify the role of diffusion of OH molecules from the interface into bulk silicon on the bonding strength in the SPAB, the silicon/silicon interface has been extensively investigated after annealing at low temperatures. Figure 6 shows the HRTEM interface images of a specimen, treated with identical plasma parameters of the specimen A3, except the O_2 RIE power (50 W) and pressure (50 Pa), after annealing at 50, 100, 150, and 225°C for 1 h in air.¹⁸ The HRTEM images showed intermediate amorphous layers across all the interfaces. The thicknesses of the amorphous layer after annealing at 50, 100, 150, and 225°C were 3.8, 3.4, 2.8, and 3.3 nm, respectively. The decrease in the thickness of the amorphous layer from 50 to 150°C indicates absorption of hydroxyl molecules from the interface to the bulk of silicon. In contrast to the absorption behavior at 150°C, the increase in the

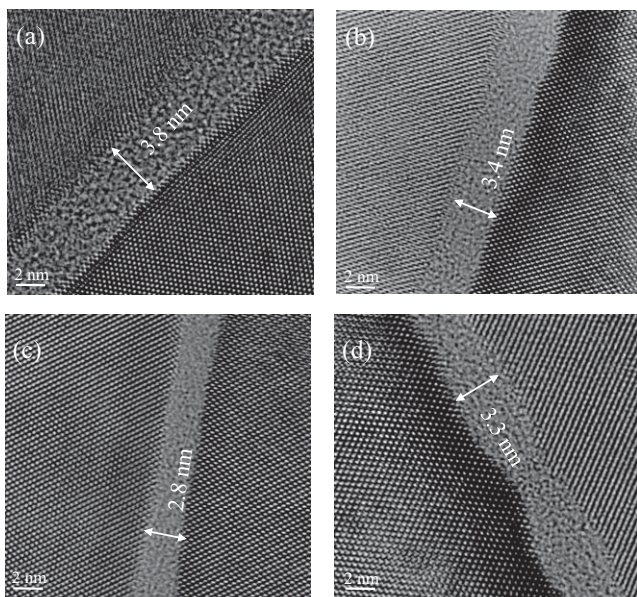


Fig. 6 HRTEM images of the Si/Si interfaces created by SPAB that were annealed at (a) 50, (b) 100, (c) 150, and (d) 225°C for 1 h in air. The sequential activation consists of a 50-W oxygen RIE plasma with time of 60 s at 50 Pa and a 2500-W MW nitrogen radical with time of 30 s at 60 Pa.¹⁸

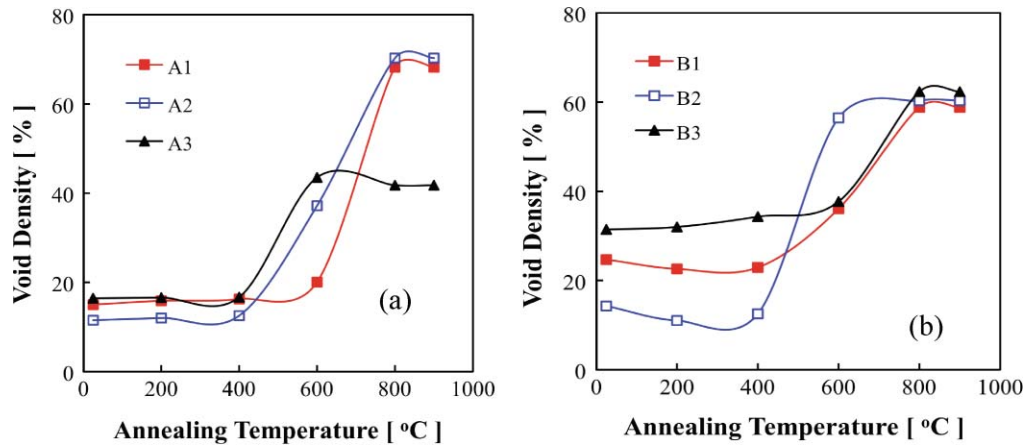


Fig. 7 Void density in the SPAB for (a) O₂ RIE time-dependent specimens (A1, A2, A3) annealed in air, and (b) O₂ RIE power-dependent specimens (B1, B2, B3) annealed in nitrogen gas for 4 h at each step.¹⁶

318 thickness of the amorphous layer was observed at 225°C.
 319 This is due to the desorption of hydroxyl molecules from
 320 the bulk of silicon to the interface. The annealing at 225°C
 321 starts producing hillocks at the interface that turn into thermal
 322 voids at higher temperatures to absorb the gas produced
 323 from the desorbed water at the interface.

3.5 Quantitative Analysis of Voids from Room Temperature to 900°C

324 As previously seen, the thermal voids were grown preferentially
 325 at plasma-induced defect sites on the activated surfaces.
 326 Therefore, the investigation of the void density associated
 327 with their transitions offers insight to the nucleated voids.
 328 Figure 7 shows the quantitative analysis of void density in
 329 the SPAB for O₂ RIE time-dependent specimens (A1, A2,
 330 A3) annealed in air [Fig. 7(a)], and O₂ RIE power-dependent
 331 specimens (B1, B2, B3) annealed in nitrogen gas as a function
 332 of annealing temperatures [Fig. 7(b)].¹⁶ Table 1 shows
 333 the plasma parameters used for the silicon surface activation
 334 for SPAB. The void density was estimated from the IR images
 335 on scaled paper. A few percents of discrepancy may exist in
 336 the estimation of the void density due to human errors. While
 337 the plasma void density remained constant up to 400°C, the
 338 thermal void density suddenly increased for all the specimens
 339 at 600°C, except for the specimen (B3) treated with an

340 thermal void density was suddenly increased for all the specimens
 341 at 600°C, except for the specimen (B3) treated with an
 342 O₂ RIE power of 400 W in nitrogen. For the B3 specimen,
 343 thermal void nucleation started at 800°C. Below 400°C, the
 344 void density for the specimens [Fig. 7(b)] annealed in N₂ gas
 345 was higher than that of the specimens [Fig. 7(a)] annealed in
 346 air. Above 600°C, the amount of thermal void density in the
 347 O₂ RIE time-dependent behavior for specimens A1 and A2
 348 was higher compared with that of the B1, B2, and B3 specimens
 349 treated with RIE power. This higher amount of void density
 350 was caused by higher activation time of N₂ radical (30 s)
 351 for specimens A1 and A2. The O₂ RIE plasma activation times
 352 for A1 and A2 were 15 and 30 s, respectively, that were not
 353 sufficient to remove native oxides and surface particles from
 354 the silicon surface. These remaining native oxides and surface
 355 particles worked as precursors for the enlargement of the voids.
 356 On the other hand, specimen A3 treated for 60 s had lower
 357 saturated void density at and above 600°C. This is attributed
 358 to the higher removal of native oxides and higher oxide
 359 thickness due to the prolonged surface activation.^{19,20}

360 The characteristic behavior of the temperature-dependent
 361 void density can be used to explain the bonding strength as a
 362 function of temperature in the SPAB of Fig. 3. A comparison
 363 between Figs. 3 and 7 showed that the bonding strength up to
 364 400°C did not change because there was no gas formation
 365 across the interface. After that, the bonding strength was
 366 reduced due to the increased amount of voids across the
 367 interface. Similar behavior of the influence of voids on bonding
 368 strength has been reported.¹⁵

3.6 Nanointerfacial Behavior at High Temperature Annealing

370 To investigate the elemental composition at the bonded inter-
 371 face after annealing, EELS was performed with the SPAB
 372 specimen sequentially heated at 600°C, shown in Fig. 8(b).
 373 The EELS experiment was performed using a field-emission
 374 TEM [JEOL (Tokyo, Japan) 2100F, C_s = 0.50 mm] in
 375 conjunction with a Gatan Enfina (Pleasanton, California)
 376 1000 spectrometer operating at 200 kV. The energy resolution
 377 was about 1.0 eV and a 1.0-nm-diam probe was used. Core-
 378 loss EELS spectra of N-K, Si-L_{2,3}, and O-K were recorded.
 379
 380

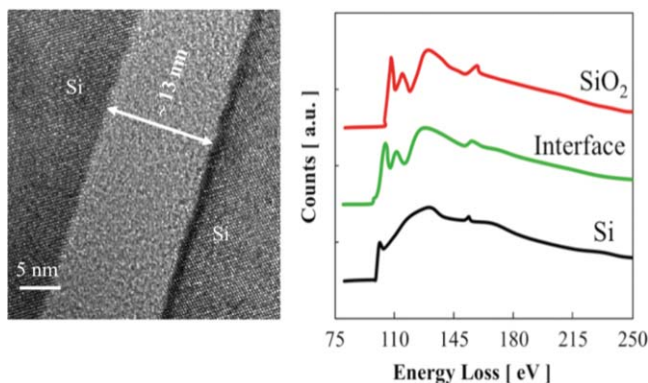


Fig. 8 Compositional distribution by EELS analysis (right) across the silicon/silicon interface (left) after sequential heating at 600°C.^{8,16}

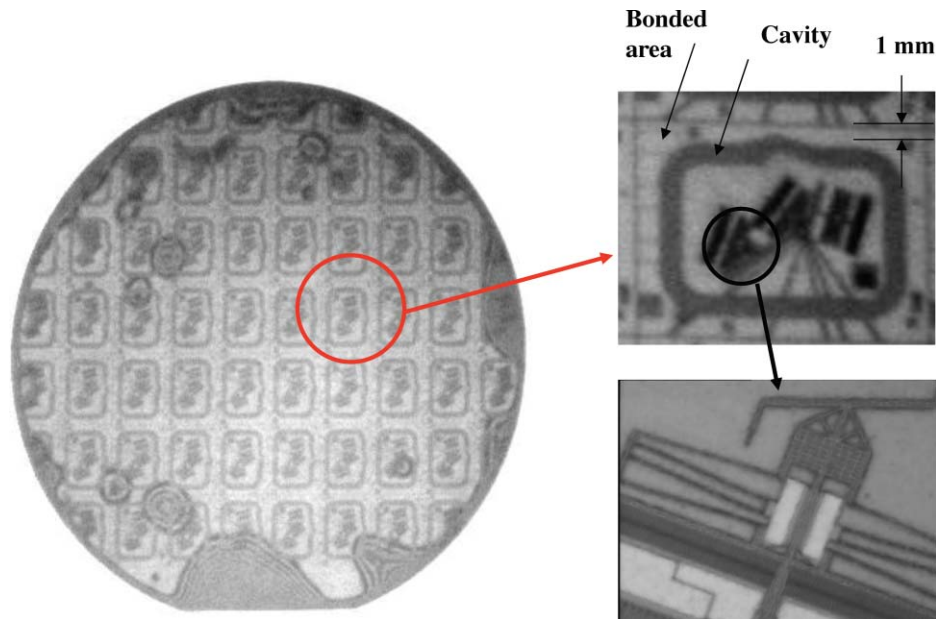


Fig. 9 IR transmission image of whole bonded area (left) and a cell (right) with selected area of bare silicon bonded with MEMS and microfluidic structured silicon after cleaning with a low-energy Ar ion source at room temperature.¹

381 From the EELS spectra, no nitrogen was detected at the
 382 bonded interface. The Si- $L_{2,3}$ edges of the 125 to 175 eV
 383 and the O-K edges at 540 to 560 eV were observed at the
 384 amorphous interface layer. To investigate the characteristic
 385 behavior of the amorphous interface layer, the Si- $L_{2,3}$ edges
 386 of the amorphous interface layer were compared with that of
 387 standard Si and SiO_2 , as shown in Fig. 8. The Si- $L_{2,3}$ edges
 388 from the amorphous interface layer were identical to those of
 389 the standard SiO_2 . Thus, the presence of SiO_2 at the interface
 390 is confirmed. This is because of the oxidation of sequentially
 391 annealed silicon at 200, 400, and 600°C for 4 h at each step
 392 in air.

393 **4 Applications of Surface-Activated Bonding and** 394 **Sequentially Plasma-Activated Bonding in** 395 **Microelectromechanical Devices and** 396 **Microfluidics**

397 **4.1 Sealing of Microelectromechanical Devices**

398 Packaging of complicated MEMS and microfluidic structures
 399 for lab-on-a chip applications, for example, requires bond-
 400 ing for substrates with silicon and silicon oxide on the same
 401 surface. The influence of silicon and silicon oxide on the
 402 same surface on the bonding quality with silicon has been
 403 investigated (Fig. 9). Although the etching rates of silicon
 404 (0.08 nm/s) and SiO_2 (0.06 nm/s) are different, there was
 405 no influence of the presence of oxide and nonoxide struc-
 406 tures on the bonding quality. The IR images show that the
 407 silicon oxides isolate microstructures from each other. The
 408 bonding experiment utilized the SAB using an Ar low-energy
 409 ion beam with 80 eV and 3 A at a background pressure of
 410 10^{-6} Pa for 60 s. The external pressure for bonding in the
 411 SAB is 0.2 MPa. The average bonding strength was above
 412 10 MPa. The low activation time resulted in strong bonding
 413 of these complicated structures with silicon.

To investigate the applicability of SAB and SPAB, the leak 414
 test and hermetic sealing behavior have been investigated. 415
 Figure 10(a) shows the leak test for silicon/glass cavities. 416
 Silicon with cavities of sizes $5.6 \times 2.4 \times 0.04$ to 0.09 mm 417
 was bonded with bare glass wafers using the SPAB. The bonded 418
 wafers were diced into chips of sizes 13×13 mm for the 419
 radioisotope fine leak test. The horizontal and vertical sealed 420
 widths of the cavity were 3.3 and 1.7 mm, respectively. The 421
 whole chip area with the cavity was 9×9 mm². A number of 422
 eight sealed cavities was exposed to a mixture of krypton-85 423
 gas of specific radioactivity of 1.6×10^{12} Bq/m³ in a back- 424
 ground high pressure of 5×10^5 Pa for 15 h to measure the 425
 leak rate of the cavities. The leak rate L (atm cc/s) of the 426
 exposed cavities was measured outside the chamber by mea- 427
 suring radiation counts coming out of the cavities using a 428
 scintillation counter. The leak rate can be estimated using 429
 the equation $L = R/skTP^2$, where R is the counts per min 430
 above ambient background, s is the specific activity of Kr 431
 gas (ci/atmcc), k is the counting efficiency of the scintillation 432
 crystal, T is the soak time (s), and P is the applied pressure 433
 (atm). The background dose was 71 to 95 cpm. The estimated 434
 leak rate was lower than 1.0×1.0^{-9} Pa · m³/s, which satisfies 435
 the requirements for Military Standards (MIL-STD)-883E 436
 encapsulation standard in hazard environments.^{2,7} 437

On the other hand, vacuum seal behavior of the cavity 438
 created by the SAB was examined by the measurements of 439
 quality factor of the cavity as a function of chamber pres- 440
 sure [Fig. 10(c)]. The quality factor (vibration characteris- 441
 tics) of a damped system can be defined by $Q = 2\pi U_i/U_d$, 442
 where U_i is the stored vibration energy and U_d is the dissi- 443
 pated energy per period. The vacuum seal cavity was fabri- 444
 cated in the following. First, a Pyrex glass wafer was 445
 bonded to silicon dioxide on a silicon wafer by anodic bond- 446
 ing. Then cavities were fabricated on the silicon side using 447
 anisotropic tetramethylammonium hydroxide (TMAH) etch- 448
 ing. Chips with cavities of $5.6 \times 2.4 \times 5$ mm³ were diced from 449

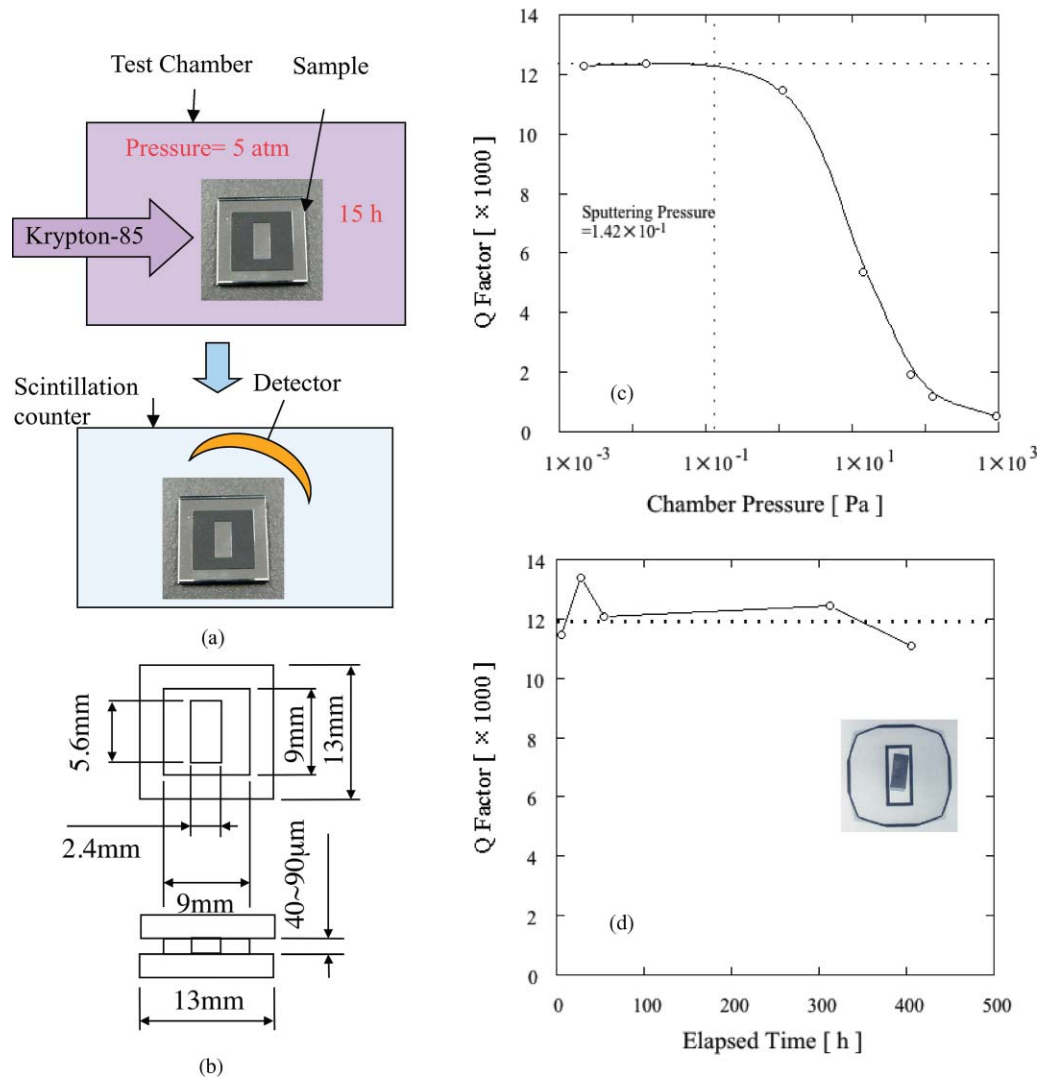


Fig. 10 (a) Schematic for radioisotope fine leak test. (b) Dimension of the bonded chip. (c) Pressure and (d) time dependence on the Q factor measured in an atomic force microscope.²

450 the fabricated silicon/glass wafers. Then a microcantilever of
 451 33-kHz resonant frequency was placed in the cavity structure
 452 and fixed on glass with indium paste to measure Q values of
 453 the cavities. The size of the cantilever was $300 \times 35 \times 2 \mu\text{m}^3$.
 454 Finally, the cavities with the cantilever were bonded with
 455 silicon (i.e., bonding between silicon and silicon). The activation
 456 energy and current were 1.5 keV and 15 mA, respectively.
 457 The activation was accomplished simultaneously using two Ar-FAB
 458 sources with 45-deg incident angles in a UHV single chamber.
 459 The time dependence of Q values of the sealed cavities was
 460 measured by using an atomic force microscope (AFM, Seiko Instruments,
 461 Incorporated, Austin, Texas, SPI3800N) [Fig. 10(d)]. The quality
 462 factor of the cavity was compared with that of the AFM vacuum
 463 chamber. The Q-dependent chamber pressure was measured using
 464 a similar cantilever in the AFM chamber [Fig. 10(c)]. The quality
 465 factors were measured through the laser beam deflection of the
 466 cantilever beams of the AFM both in the sealed cavities and
 467 AFM vacuum chamber. The quality factor of both the cavity and
 468 AFM vacuum chamber corresponds to the vacuum pressure inside
 469 the cavity. Identical Q values at the
 470

reference vacuum level at the time of surface activation and
 cavities were observed. This is indicative of air-tight cavities.
 However, the leak rate (\sim quantity of air in cubic meters
 flowing through a leak per second) of the vacuum-sealed
 cavities was estimated from the difference between the maximum
 and minimum Q values and the cavity volume (cantilever
 volume was deducted). The estimated leak rate was
 $2.6 \times 10^{-16} \text{ Pa m}^3/\text{s}$ after 400 h, which was much lower
 than the American MIL STD for hermetic sealing in hazardous
 environments.

4.2 Reliability in Microfluidics

Figures 11(a) and 11(b) show the IR images of a whole
 4-in. wafer and two cavities out of 180 in a cell, respectively.
 Figure 11(c) shows the cross sectional scanning electron
 microscope (SEM) image of the bonded interface. The wafer
 has a total number of 46 cells. Each cell has 180 cavities.
 Each cavity has 11.5-mm-long, 180- μm -deep, and 20- μm -
 wide channels. The space between two bonded channels is
 40 μm . After the fabrication of deep channels, a 20- μm -thick

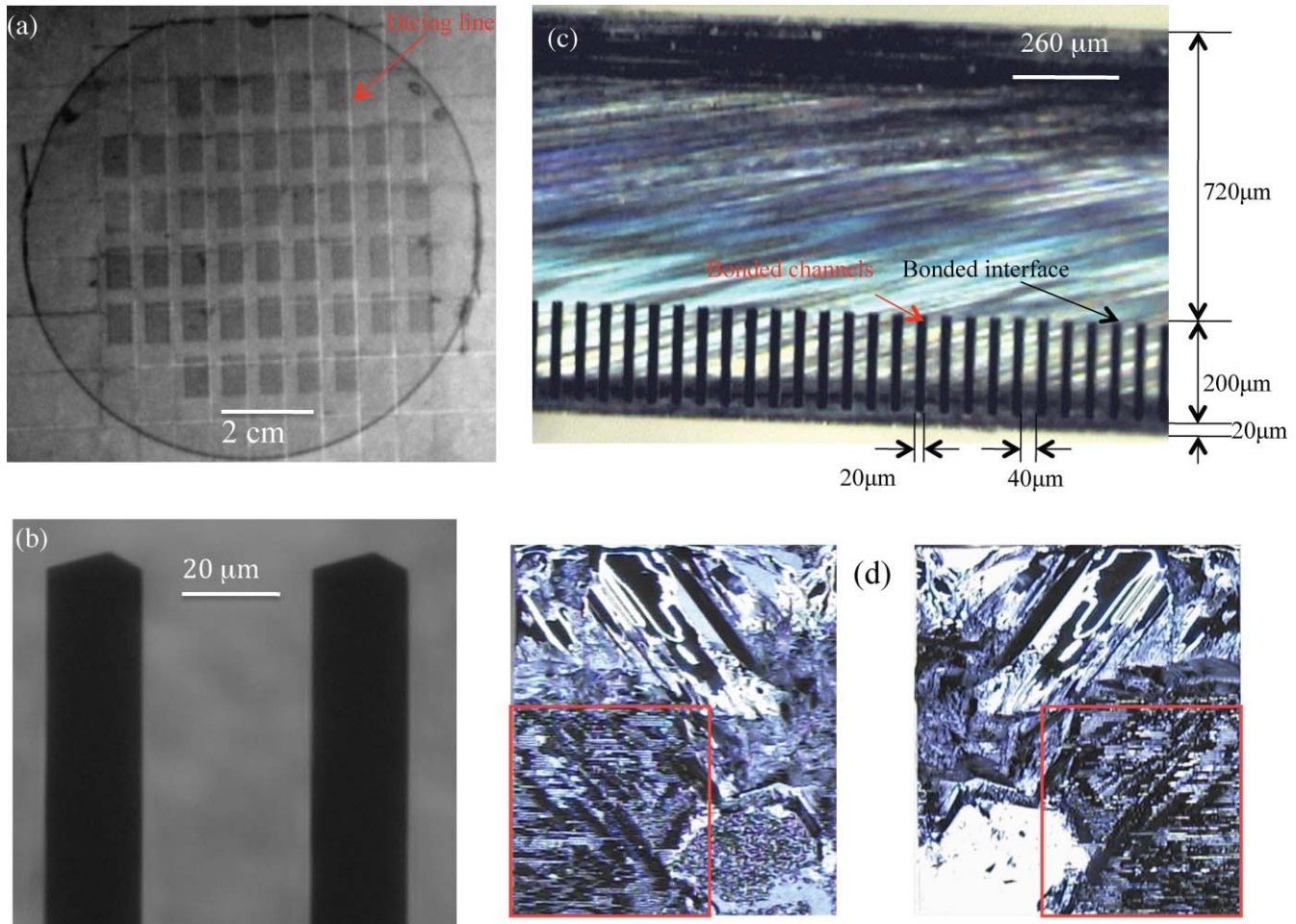


Fig. 11 Images of microfluidic channels in silicon after bonding with bare silicon. (a) IR image of the whole bonded interface. (b) IR image of two cavities out of 180 in a cell. (c) Cross sectional scanning electron microscope (SEM) image of the bonded interface. (d) Fracture images of the bonded interface after tensile pulling tests.²¹

490 silicon layer is left after making the channels on a 200- μm -
 491 thick silicon wafer. The dicing places are seen on the bonded
 492 area as white lines. The IR images of the cell areas are black
 493 because of the sealed channels in the cell. No visible voids
 494 were seen across the bonding interface among fine channels
 495 [Figs. 11(a) and 11(b)]. Figure 11(d) shows the fracture im-
 496 ages of the bonded interfaces of bare/microfluidic structure
 497 wafers after tensile pulling tests.²¹ The marked area is the
 498 bonding area with fine patterns and the rest is a bare bonded
 499 area. The fracture images show bulk fractures both in bare
 500 and patterned regions. The bonded interface can be useful
 501 for microfluidic channels and reservoir applications where
 502 micro/nanoliters¹ of liquid may be required and externally
 503 pumped with strong pressure into the working area.

504 For chemical reliability observation, the bonding strength
 505 of the silicon/silicon interfaces prepared by the SAB and
 506 SPAB after dipping in water, ethanol, acetone, and 3% HF for
 507 30 days at room temperature has been measured, as shown in
 508 Fig. 12(a). Three bars represent the data for three specimens.
 509 The bonding strength showed considerable dependence on
 510 the chemical types. The bonding strength in the SPAB was
 511 higher than that in the SAB, except for dipping in HF. The
 512 bonding strength in the SPAB was not noticeably degraded
 513 in HF. The considerable difference in the bonding strength

of the SAB and plasma-processed interfaces dipped in HF
 was controlled by different chemical compositions at the
 interfaces.

Figure 12(b) shows the bonding strength of silicon/silicon
 bonded interfaces in the SAB and SPAB at room temper-
 ature as a function of dipping time in 3% HF acid. The
 bonding strength decreased with the increase of HF dip time.
 The bonding strength for SAB-processed interfaces remained
 constant for 20 days. In the SAB, silicon wafers were acti-
 vated with an Ar low-energy ion source of 80 V and 3 A
 for 10 s, and bonded in a vacuum pressure of 10^{-7} Pa. In
 the SPAB, the wafers were activated with O₂ RIE and N₂
 radicals each for 60 s and bonded under hand-applied pres-
 sure. In the SAB, the bonding strength remained constant for
 20 days and then decreased with the increase of dipping time.
 In the SPAB, the bonding strength decreased in the increase
 of dipping time from the beginning of the experiments. This
 time-dependent discrepant behavior can be explained using
 the chemical compositions across the interface. Faster de-
 crease of the silicon/silicon bonding strength in the SPAB
 was due to the etching of oxides and the presence of voids
 across the interface. On the other hand, such oxides are not
 present in the SAB, and resulted in lesser etching than the
 SPAB interface.

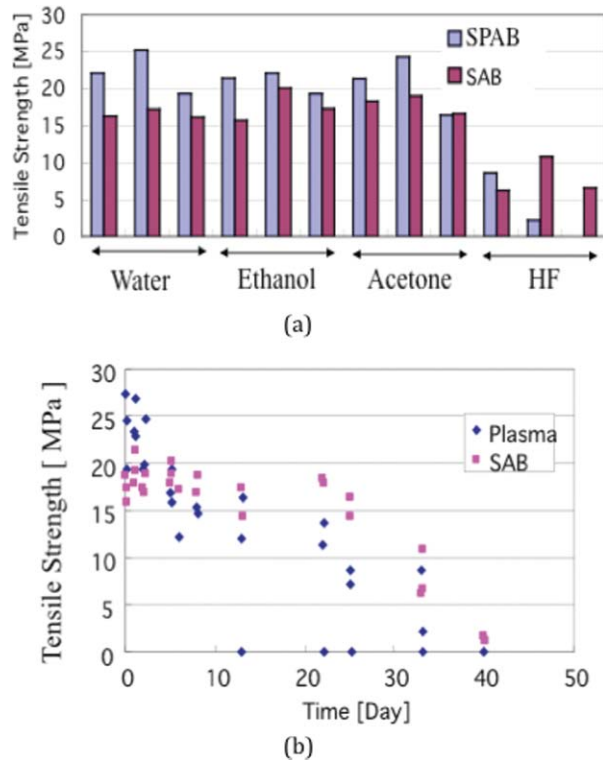


Fig. 12 (a) Bonding strength of silicon/silicon as a function of dipping in (a) various chemicals and (b) time in 3% hydrofluoric acid at room temperature.⁷

5 Conclusions

A comprehensive review of surface-activated bonding (SAB) compared with sequentially plasma-activated bonding (SPAB) is given with applications for packaging microelectromechanical systems (MEMS) and microfluidic devices. The bonding strength of the interface in the SAB and SPAB is as high as that of conventional hydrophilic bonding methods, which require annealing as high as 1000°C to achieve covalent bonding. Before heating, a void-free interface is achieved in SAB, a considerable number of voids are observed in the SPAB, which is due to the plasma-induced surface defects. After heating, voids are not observed and bonding strengths are not changed in the SAB. On the other hand, increase in interfacial voids with annealing temperatures is observed, which decreases the bonding strength in the SPAB. Although the rearrangement of water such as absorption and desorption across the bonded interface is found below 225°C, the voids are not significant up to 400°C. Annealing above 600°C results in a considerable amount of thermal voids due to the viscous flow of oxides. Amorphous layers with thicknesses of 8.3 and 4.6 nm are observed at interfaces in the SAB and SPAB, respectively, before heating. These disappear and enlarge in SAB and SPAB, respectively, after heating. Electron energy loss spectroscopy shows the presence of SiO₂ in the nanointerfacial amorphous layer due

to oxidation of the silicon/silicon interface after sequential heating. The bonding strength, sealing, and chemical performances of the interfaces meet the requirements for microelectromechanical systems and microfluidics applications.

Acknowledgments

This research was supported by a discovery grant (number 327947) from the Natural Science and Engineering Research Council of Canada, and an infrastructure grant (number 12128) from the Canada Foundation for Innovation (CFI). Jamal Deen is greatly thanked for his support and assistance in establishing nanobonding and interconnection research at the Micro- and Nano-Systems Laboratory at McMaster University. Moon J. Kim from the University of Texas at Dallas is thanked for the contribution in the high resolution transmission electron microscopy experiments. Fangfang Zhang and M. G. Kibria are greatly acknowledged for their assistance in the preparation of the manuscript.

References

- M. M. R. Howlader and T. Suga, *Proc. Electron. Comp. Technol. Conf.*, pp. 1423–1429 (2009).
- M. M. R. Howlader, H. Okada, T. H. Kim, T. Itoh, and T. Suga, *J. Electrochem. Soc.* **151**(7), G461–G467 (2004).
- S. H. Choa, *Microelectron. Reliab.* **45**, 361–369 (2005).
- T. Itoh and T. Suga, *J. Micromech. Microeng.* **15**, S281–S285 (2005).
- W. B. Yu, C. M. Tan, J. Wei, S. S. Deng, and S. M. L. Nai, *Sens. Actuators A* **115**, 67–72 (2004).
- S. C. Johnston, *Semicon. Int.* **30**(1), 34 (2007).
- M. M. R. Howlader, S. Suehara, H. Takagi, T. H. Kim, R. Maeda, and T. Suga, *IEEE Trans. Adv. Packag.* **29**, 448–456 (2006).
- M. G. Kibria, F. Zhang, T. H. Lee, M. J. Kim, and M. M. R. Howlader, *Nanotechnol.* **21**(13), 134011 (2009).
- M. Bruel, *Nucl. Instr. Meth. Phys. Res. B* **108**, 313 (1996).
- M. M. R. Howlader, T. Suga, H. Itoh, T. H. Lee, and M. J. Kim, *J. Electrochem. Soc.* **156**, H846–H851 (2009).
- M. M. R. Howlader, T. Suga, H. Itoh, and M. J. Kim, *ECS Trans.* **3**, 191–202 (2006).
- Q. Y. Tong and U. Gosele, *Semiconductor Wafer Bonding*, p. 52, Wiley, New York (1999).
- M. M. R. Howlader, M. G. Kibria, and F. Zhang, *Thin Solid Films* (in press).
- M. Shimbo, K. Furukawa, K. Fukuda, and K. Tanzawa, *J. Appl. Phys.* **60**(8), 2987–2989 (1986).
- X. X. Zhang and J. P. Raskin, *J. Microelectromech. Sys.* **14**, 368–382 (2005).
- M. M. R. Howlader, F. Zhang, and M. G. Kibria, *J. Micromech. Microeng.* **20**(6), 065012 (2010).
- M. Eichler, B. Michel, M. Thomas, M. Gabriel, and C. P. Klages, *Surf. Coat. Technol.* **203**, 826–829 (2008).
- M. M. R. Howlader, G. Kagami, T. H. Lee, J. G. Wang, M. J. Kim, and A. Yamauchi, *J. Microelectromech. Syst.* **19**(4), 840–848 (2010).
- V. Dragoi, G. Mittendorfer, C. Thanner, and P. Lindner, *Microsystem Tech.* **14**, 509–515 (2008).
- M. Eichler, B. Michel, P. Hennecke, and C. P. Klages, *J. Electrochem. Soc.* **156**, H786–H793 (2009).
- D. Pasquariello, C. Hedlund, and K. Hijort, *J. Electrochem. Soc.* **147**(7), 2699–2703 (2000).
- S. Bengtsson and P. Amirfeiz, *J. Electron. Mat.* **29**, 909–915 (2000).
- A. Weinert, P. Amirfeiz, and S. Bengtsson, *Sens. Actuators A* **A92**, 214–222 (2001).
- C. Yang, U. Tartaglino, and B. N. J. Persson, *Phys. Rev. Lett.* **97**, 116103–11604 (2006).
- X. Ma, C. Chen, W. Liu, X. Liu, X. Du, Z. Song, and C. Lin, *J. Electrochem. Soc.* **156**, H307–H310 (2009).

625
626
627
628
629
630
631
632
633
634
635
636
637
638
639
640
641
642
643
644
645
646
647
648
649



Dr. Matiar M. R. Howlader received the BScEng degree in electrical and electronic engineering from Khulna University of Engineering and Technology, Khulna, Bangladesh, in 1988, and the MS and PhD degrees in nuclear engineering from Kyushu University, Fukuoka, Japan, in 1996 and 1999, respectively. From 2000 to 2005, he was with the Research Center for Advanced Science and Technology, The University of Tokyo, Japan, as an endowed associate professor. He is currently an assistant professor in the Department of Electrical and Computer Engineering, McMaster University, Hamilton, Ontario, Canada. His research focuses on chip-size and wafer-level planar and vertical integration for microelectronics, microelectromechanical systems, and optoelectronics packaging, oxidation behavior of solders and electronic materials, interfacial adhesions, and radiation effects on materials and packages. He has started a new initiative on nanobonding and packaging of materials, devices, and components for microsystems and nanosystems for health and environmental applications. He has published more than 40 refereed papers and more than 65 international proceedings articles. He is a member of the Japan Institute of Electronic Packaging. He was the recipient of the Best Technical Paper Award at the International Conference on Electronic Packaging in 2003.



Tadatomo Suga received the MS degree in precision engineering from the University of Tokyo in 1979. He joined the Max-Planck Institut für Metallforschung, Stuttgart, in 1979, and received the PhD degree from the University of Stuttgart in 1983 for his study on fracture mechanics characterization of metal-ceramic interfaces. In 1984 he became a member of the Faculty of Engineering at the University of Tokyo, and since 1993, he has been a professor of precision engineering. He is also conducting a research group at the National Institute of Materials Science (NIMS) in Tsukuba as a director, and he is a member of the Science Council of Japan. His research focuses on microsystems integration and packaging, and development of interconnect technology, especially room temperature bonding techniques for various applications. He has published 200 papers and five books in the field of material science and electronic packaging.

650
651
652
653
654
655
656
657
658
659
660
661
662
663
664
665
666
667